Supplementary Information

Subcycle switching reveals the intraband origin of low-order harmonics in a dielectric

Shanming Chen, Shidong Yang, Xun Cong, Hongwei Zang, Yu Jiang, Helong Li, Xiaohong Song, Matthias Reichelt, Torsten Meier, Weifeng Yang and Huailiang Xu

Supplementary Note 1 | Full-polarization decomposition of the semiconductor current

The nonlinear optical response of solids is commonly described using a mixed formulation in which interband dynamics are expressed in terms of a polarization, whereas intraband dynamics are introduced directly as a current. In this framework, interband harmonics arise from coherent superpositions of valence- and conduction-band states and are naturally associated with a polarization, while intraband harmonics are attributed to carrier motion within a band and are treated at the level of current from the outset[1,2]. However, this practical asymmetric decomposition is not fundamental and, as we show below, can obscure cancellations that are essential for identifying observable radiation channels.

Perfect crystalline solids are infinite periodic systems which leads to subtleties when evaluating the position operator. For localized states, the matrix elements of the position operator are well defined and can be computed straightforwardly. In a crystal, however, the electronic eigenstates are extended Bloch functions and the absolute position of an electron is not a uniquely defined quantity under periodic boundary conditions[3]. The modern theory of polarization resolves this difficulty by emphasizing that changes in polarization, rather than the absolute position itself, are the measurable quantities[4]. During a continuous evolution under an external electric field, an electronic wave packet may be regarded as moving relative to a reference Wannier center. This relative displacement is single-valued and physically meaningful, independent of the choice of the initial Wannier center. It is this change of polarization, or equivalently the current, that provides a consistent description of charge motion in a periodic solid.

The length-gauge formulation of Aversa and Sipe provides a concrete realization of this principle for semiconductor response functions[5]. In this formulation, interband and intraband contributions are treated on the same footing: both are obtained from the time derivative of the polarization. We write the length-gauge Hamiltonian as

$$\hat{H}(t) = \hat{H}_0 - q_e\,\mathbf{E}(t)\cdot\hat{\mathbf{r}}, \tag{S1}$$

The one-particle density operator obeys

$$i\hbar\frac{d\hat{\rho}}{dt} = [\hat{H},\hat{\rho}]. \tag{S2}$$

Following Aversa and Sipe, the position operator is decomposed into its intraband and interband parts,

$$\hat{\mathbf{r}} = \hat{\mathbf{r}}_i + \hat{\mathbf{r}}_e. \tag{S3}$$

Here the subscript i denotes the intraband part and the subscript e denotes the interband part. For Bloch states $|n\mathbf{k}\rangle$, the corresponding matrix elements are

$$\langle n\mathbf{k}|\hat{\mathbf{r}}_i|m\mathbf{k}'\rangle = \delta_{nm}\left[\boldsymbol{\xi}_{nn}(\mathbf{k})\delta(\mathbf{k}-\mathbf{k}') + i\nabla_{\mathbf{k}}\delta(\mathbf{k}-\mathbf{k}')\right], \tag{S4}$$

$$\langle n\mathbf{k}|\hat{\mathbf{r}}_e|m\mathbf{k}'\rangle = (1-\delta_{nm})\boldsymbol{\xi}_{nm}(\mathbf{k})\delta(\mathbf{k}-\mathbf{k}'), \tag{S5}$$

where

$$\boldsymbol{\xi}_{nm}(\mathbf{k}) = i\langle u_{n\mathbf{k}}|\nabla_{\mathbf{k}} u_{m\mathbf{k}}\rangle_{\text{cell}} = \frac{i}{\Omega_{\text{cell}}}\int_{\Omega_{\text{cell}}} u^*_{n\mathbf{k}}(\mathbf{r})\,\nabla_{\mathbf{k}} u_{m\mathbf{k}}(\mathbf{r})\,d\mathbf{r}. \tag{S6}$$

is the Berry-connection matrix element, and Ω_{cell} is the unit-cell volume.

Although the intraband position operator $\hat{\mathbf{r}}_{\text{i}}$ has singular matrix elements in a crystal, its commutator with a simple operator is itself simple. Here a "simple" operator $\hat{S}$ is one whose Bloch matrix elements contain only $\delta(\mathbf{k}-\mathbf{k}')$, i.e.

$$\langle n\mathbf{k}|\hat{S}|m\mathbf{k}'\rangle = S_{nm}(\mathbf{k})\,\delta(\mathbf{k}-\mathbf{k}'). \tag{S7}$$

In this case one obtains

$$\langle n\mathbf{k}|[\hat{\mathbf{r}}_{\text{i}}, \hat{S}]|m\mathbf{k}'\rangle = i\,\delta(\mathbf{k}-\mathbf{k}')\,(S_{nm})_{;\mathbf{k}}, \tag{S8}$$

where

$$(S_{nm})_{;\mathbf{k}} = \nabla_{\mathbf{k}} S_{nm} - i(\boldsymbol{\xi}_{nn} - \boldsymbol{\xi}_{mm})S_{nm} \tag{S9}$$

is the generalized derivative. This result avoids the careful limiting procedures that would otherwise be required by the singular matrix elements of $\hat{\mathbf{r}}_{\text{i}}$. Importantly, although the ordinary k-derivative and the diagonal Berry connections are not separately gauge invariant, their combination in Eq. (S9) transforms covariantly under band-dependent phase changes and leads to gauge-independent traces and currents.

The total polarization current is obtained from the time derivative of the total polarization,

$$\boldsymbol{J}(t) = \frac{d\boldsymbol{P}(t)}{dt} = q_e \text{Tr}\left(\hat{\boldsymbol{v}}\hat{\rho}\right), \tag{S10}$$

where the length-gauge velocity operator is

$$\hat{\boldsymbol{v}} = \frac{1}{i\hbar}[\hat{\boldsymbol{r}}, \hat{H}]. \tag{S11}$$

Using the Aversa–Sipe decomposition $\hat{\boldsymbol{r}} = \hat{\boldsymbol{r}}_{\text{i}} + \hat{\boldsymbol{r}}_{\text{e}}$, the current can be written as

$$\begin{aligned}\boldsymbol{J}(t) &= \frac{d}{dt}\left[\boldsymbol{P}_{\text{intra}}(t) + \boldsymbol{P}_{\text{inter}}(t)\right] \\ &= \underbrace{\frac{q_e}{i\hbar}\text{Tr}\left([\hat{\boldsymbol{r}}_{\text{i}}, \hat{H}]\hat{\rho}\right)}_{\boldsymbol{J}^{\text{pol}}_{\text{intra}}(t)} + \underbrace{\frac{q_e}{i\hbar}\text{Tr}\left([\hat{\boldsymbol{r}}_{\text{e}}, \hat{H}]\hat{\rho}\right)}_{\boldsymbol{J}^{\text{pol}}_{\text{inter}}(t)}.\end{aligned} \tag{S12}$$

Thus the intra- and interband responses are both defined here as polarization currents, rather than treating one at the current level and the other at the polarization level.

We now expand the two terms in Eq. (S12). For the intraband part,

$$\begin{aligned}\boldsymbol{J}^{\text{pol}}_{\text{intra}}(t) &= \frac{q_e}{i\hbar}\text{Tr}\left([\hat{\boldsymbol{r}}_{\text{i}}, \hat{H}_0]\hat{\rho}\right) + \frac{q_e}{i\hbar}\text{Tr}\left([\hat{\boldsymbol{r}}_{\text{i}}, -q_e\boldsymbol{E}(t)\cdot\hat{\boldsymbol{r}}_{\text{i}}]\hat{\rho}\right) \\ &\quad + \frac{q_e}{i\hbar}\text{Tr}\left([\hat{\boldsymbol{r}}_{\text{i}}, -q_e\boldsymbol{E}(t)\cdot\hat{\boldsymbol{r}}_{\text{e}}]\hat{\rho}\right) \\ &\equiv \boldsymbol{J}^{\text{conv}}_{\text{intra}}(t) + \boldsymbol{J}^{\text{anom}}_{\text{intra}}(t) + \boldsymbol{J}^{\text{inj-like}}_{\text{intra}}(t).\end{aligned} \tag{S13}$$

Similarly, the interband-polarization current gives

$$\begin{aligned}\boldsymbol{J}^{\text{pol}}_{\text{inter}}(t) &= \frac{q_e}{i\hbar}\text{Tr}\left([\hat{\boldsymbol{r}}_{\text{e}}, \hat{H}_0]\hat{\rho}\right) + \frac{q_e}{i\hbar}\text{Tr}\left([\hat{\boldsymbol{r}}_{\text{e}}, -q_e\boldsymbol{E}(t)\cdot\hat{\boldsymbol{r}}_{\text{e}}]\hat{\rho}\right) \\ &\quad + \frac{q_e}{i\hbar}\text{Tr}\left([\hat{\boldsymbol{r}}_{\text{e}}, -q_e\boldsymbol{E}(t)\cdot\hat{\boldsymbol{r}}_{\text{i}}]\hat{\rho}\right) \\ &\equiv \boldsymbol{J}^{\text{conv}}_{\text{inter}}(t) + \boldsymbol{J}^{\text{self}}_{\text{inter}}(t) + \boldsymbol{J}^{\text{inj-like}}_{\text{inter}}(t).\end{aligned} \tag{S14}$$

Eqs. (S13) and (S14) show that treating the intra- and interband parts of the position operator on the same polarization-current footing naturally gives three terms in each current. The first terms are the conventional intra- and interband currents, with

$$\boldsymbol{J}^{\mathrm{conv}}_{\mathrm{intra}}(t) = \frac{q_e}{i\hbar}\mathrm{Tr}\left([\hat{\boldsymbol{r}}_{\mathrm{i}}, \hat{H}_0]\hat{\rho}\right) = q_e \sum_{n,\boldsymbol{k}} \rho_{nn}(\boldsymbol{k},t)\boldsymbol{v}_n(\boldsymbol{k}), \qquad \boldsymbol{v}_n(\boldsymbol{k}) = \frac{1}{\hbar}\nabla_{\boldsymbol{k}}\varepsilon_n(\boldsymbol{k}), \tag{S15a}$$

$$\boldsymbol{J}^{\mathrm{conv}}_{\mathrm{inter}}(t) = \frac{q_e}{i\hbar}\mathrm{Tr}\left([\hat{\boldsymbol{r}}_{\mathrm{e}}, \hat{H}_0]\hat{\rho}\right) = \frac{q_e}{i\hbar}\sum_{\boldsymbol{k}}\sum_{n\neq m}\left[\varepsilon_m(\boldsymbol{k}) - \varepsilon_n(\boldsymbol{k})\right]\rho_{mn}(\boldsymbol{k},t)\boldsymbol{\xi}_{nm}(\boldsymbol{k}). \tag{S15b}$$

The remaining terms are field-dependent commutator contributions generated by the length-gauge light–matter coupling. The self-commutator term in the intraband polarization current,

$$\boldsymbol{J}^{\mathrm{anom}}_{\mathrm{intra}}(t) = \frac{q_e}{i\hbar}\mathrm{Tr}\left([\hat{\boldsymbol{r}}_{\mathrm{i}}, -q_e\boldsymbol{E}(t)\cdot\hat{\boldsymbol{r}}_{\mathrm{i}}]\hat{\rho}\right) = -\frac{q_e^2}{\hbar}\sum_{n,\boldsymbol{k}}\rho_{nn}(\boldsymbol{k},t)\,\boldsymbol{E}(t)\times\boldsymbol{\Omega}_n(\boldsymbol{k}), \tag{S16a}$$

with $\boldsymbol{\Omega}_n(\boldsymbol{k}) = \nabla_{\boldsymbol{k}}\times\boldsymbol{\xi}_{nn}(\boldsymbol{k})$ is the Berry curvature of band n. Equivalently, the corresponding single-particle anomalous velocity is

$$\boldsymbol{v}^{\mathrm{anom}}_n(\boldsymbol{k},t) = -\frac{q_e}{\hbar}\boldsymbol{E}(t)\times\boldsymbol{\Omega}_n(\boldsymbol{k}). \tag{S16b}$$

This term is a band-geometric contribution and has no counterpart in the free-electron polarization current of atomic media which will be discussed in the following section.

The interband polarization current also contains an analogous self-commutator term,

$$\boldsymbol{J}^{\mathrm{self}}_{\mathrm{inter}}(t) = \frac{q_e}{i\hbar}\mathrm{Tr}\left([\hat{\boldsymbol{r}}_{\mathrm{e}}, -q_e\boldsymbol{E}(t)\cdot\hat{\boldsymbol{r}}_{\mathrm{e}}]\hat{\rho}\right) = -\frac{q_e^2}{\hbar}\sum_{n,m,\boldsymbol{k}}\rho_{mn}(\boldsymbol{k},t)\,\boldsymbol{E}(t)\times\boldsymbol{\Omega}^{ee}_{nm}(\boldsymbol{k}), \tag{S17a}$$

with

$$\boldsymbol{\Omega}^{ee}_{nm}(\boldsymbol{k}) = -i\sum_l \boldsymbol{\xi}_{nl,\mathrm{e}}(\boldsymbol{k})\times\boldsymbol{\xi}_{lm,\mathrm{e}}(\boldsymbol{k}). \tag{S17b}$$

We next consider the mixed commutator terms generated by the intra- and interband polarization currents. The mixed term from the intraband polarization current is

$$\begin{aligned}\boldsymbol{J}^{\mathrm{inj-like}}_{\mathrm{intra}}(t) &= \frac{q_e}{i\hbar}\mathrm{Tr}\left([\hat{\boldsymbol{r}}_{\mathrm{i}}, -q_e\boldsymbol{E}(t)\cdot\hat{\boldsymbol{r}}_{\mathrm{e}}]\hat{\rho}\right)\\ &= -\frac{q_e^2}{\hbar}\sum_{n\neq m,\boldsymbol{k}}\rho_{mn}(\boldsymbol{k},t)\left[\boldsymbol{E}(t)\cdot\boldsymbol{\xi}_{nm}(\boldsymbol{k})\right]_{;\boldsymbol{k}},\end{aligned} \tag{S18a}$$

where

$$\left[\boldsymbol{E}(t)\cdot\boldsymbol{\xi}_{nm}\right]_{;\boldsymbol{k}} = \nabla_{\boldsymbol{k}}\left[\boldsymbol{E}(t)\cdot\boldsymbol{\xi}_{nm}\right] - i\left(\boldsymbol{\xi}_{nn} - \boldsymbol{\xi}_{mm}\right)\left[\boldsymbol{E}(t)\cdot\boldsymbol{\xi}_{nm}\right]. \tag{S18b}$$

The corresponding mixed term from the interband polarization current is

$$\begin{aligned}\boldsymbol{J}^{\mathrm{inj-like}}_{\mathrm{inter}}(t) &= \frac{q_e}{i\hbar}\mathrm{Tr}\left([\hat{\boldsymbol{r}}_{\mathrm{e}}, -q_e\boldsymbol{E}(t)\cdot\hat{\boldsymbol{r}}_{\mathrm{i}}]\hat{\rho}\right)\\ &= \frac{q_e^2}{\hbar}\sum_{n\neq m,\boldsymbol{k}}\rho_{mn}(\boldsymbol{k},t)\left[\boldsymbol{E}(t)\cdot\nabla_{\boldsymbol{k}} - i\boldsymbol{E}(t)\cdot\left(\boldsymbol{\xi}_{nn} - \boldsymbol{\xi}_{mm}\right)\right]\boldsymbol{\xi}_{nm}(\boldsymbol{k}).\end{aligned} \tag{S19a}$$

Equivalently, the component forms are

$$J^{\mathrm{inj-like}}_{\mathrm{intra},\alpha}(t) = -\frac{q_e^2}{\hbar}\sum_{n\neq m,\boldsymbol{k}}\rho_{mn}(\boldsymbol{k},t)\sum_\beta E_\beta(t)\left(\xi^\beta_{nm}\right)_{;k_\alpha}, \tag{S19b}$$

and

$$J^{\mathrm{inj-like}}_{\mathrm{inter},\alpha}(t) = +\frac{q_e^2}{\hbar}\sum_{n\neq m,\boldsymbol{k}} \rho_{mn}(\boldsymbol{k},t)\sum_{\beta} E_\beta(t)\,(\xi^{\alpha}_{nm})_{;k_\beta}\,. \tag{S19c}$$

The different index order in Eqs. (S19b) and (S19c) reflects which position operator carries the observed current component. For a linearly polarized field, $\boldsymbol{E}(t) = E(t)\hat{\boldsymbol{e}}_\parallel$, $J_\parallel(t) = \hat{\boldsymbol{e}}_\parallel \cdot \boldsymbol{J}(t)$, the sum of the two mixed terms projected along the driving field (i.e., $\alpha = \beta$) is

$$J^{\mathrm{inj-like}}_{\mathrm{intra},\parallel}(t) + J^{\mathrm{inj-like}}_{\mathrm{inter},\parallel}(t) = 0. \tag{S20}$$

Thus, the tunnelling-injection-like contribution cancels from the field-projected current.

For a transverse current component (i.e., $\alpha \neq \beta$), $J_\perp = \hat{\boldsymbol{e}}_\perp \cdot \boldsymbol{J}$, with $\hat{\boldsymbol{e}}_\perp \cdot \hat{\boldsymbol{e}}_\parallel = 0$, their sum is

$$J^{\mathrm{inj-like}}_{\mathrm{intra},\perp}(t) + J^{\mathrm{inj-like}}_{\mathrm{inter},\perp}(t) = \frac{q_e^2}{\hbar}\sum_{n\neq m,\boldsymbol{k}} \rho_{mn}\sum_{\alpha\beta} \hat{e}_{\perp,\alpha} E_\beta(t)\left[(\xi^{\alpha}_{nm})_{;k_\beta} - \left(\xi^{\beta}_{nm}\right)_{;k_\alpha}\right]. \tag{S21a}$$

The bracket is the covariant curl of the interband Berry-connection matrix element. More generally,

$$(\xi^{\alpha}_{nm})_{;k_\beta} - \left(\xi^{\beta}_{nm}\right)_{;k_\alpha} = i\sum_{l\neq n,m}\left(\xi^{\beta}_{nl}\xi^{\alpha}_{lm} - \xi^{\alpha}_{nl}\xi^{\beta}_{lm}\right). \tag{S21b}$$

When this covariant curl vanishes, the transverse mixed terms cancel as well. According to Eq. (S21b), a residual can occur only when remote bands are explicitly retained in a multiband description and provide nonzero intermediate-band couplings. Such a residual, if present, is not a tunnelling-injection-like current, but a geometric transverse response, contributing to emission perpendicular to the laser polarization and to symmetry-allowed even-order harmonics. In the closed two-band model, there is no intermediate band $l \neq c, v$, and therefore

$$(\xi^{\alpha}_{cv})_{;k_\beta} = \left(\xi^{\beta}_{cv}\right)_{;k_\alpha}. \tag{S21c}$$

Consequently,

$$J^{\mathrm{inj-like}}_{\mathrm{intra},\perp}(t) + J^{\mathrm{inj-like}}_{\mathrm{inter},\perp}(t) = 0. \tag{S21d}$$

Thus, the intra- and interband injection-like terms cancel for any current component in this case, including components both parallel and perpendicular to the laser polarization.

Supplementary Note 2 | Tunnelling-injection analogy in the intraband polarization current

The physical intuition behind an injection current can be traced to the polarization of electrons set free by field ionization in atoms or gases, where the position operator is well defined. For free electrons with density $n_e(t)$ and position $\mathbf{x}(t)$, one may write from semiclassical considerations[6]

$$\mathbf{P}_{\mathrm{free}}(t) = q_e n_e(t)\mathbf{x}(t). \tag{S22}$$

The corresponding current is

$$\mathbf{J}_{\mathrm{free}}(t) = \frac{d\mathbf{P}_{\mathrm{free}}}{dt} = q_e\dot{n}_e(t)\mathbf{x}(t) + q_e n_e(t)\mathbf{v}(t). \tag{S23}$$

The first term arises when new charge is created at a finite birth position. The second term is the ordinary current of already liberated electrons. If the electron is born at a tunnel-exit displacement $\mathbf{x}_0$, the first term can be approximated by $q_e\dot{n}_e(t)\mathbf{x}_0$, since $\dot{n}_e(t) \neq 0$ only when a

free electron is born. This term is the origin of the tunneling injection term adopted in Ref.[7]. The resulting emitted field which is proportional to the time derivative of the associated current is

$$\dot{\mathbf{J}}_{\text{free}}(t) = \frac{d}{dt}[q_e \dot{n}_e(t)\mathbf{x}_0] + q_e \dot{n}_e(t)\mathbf{v}_0(t) + q_e n_e(t)\dot{\mathbf{v}}(t). \tag{S24}$$

Since $\ddot{\mathbf{x}}(t) = \dot{\mathbf{v}}(t) = q_e\mathbf{E}(t)$, the third term can be written as $q_e^2 n_e(t)\mathbf{E}(t)$, which is the Brunel emission term[8,9].

In a solid, interband tunnelling from a valence band to a conduction band is superficially analogous to the liberation of an electron into the continuum. Therefore, the polarization of continuum free electrons in atomic media can be naturally viewed as the analogue of the conduction-band electron polarization in solids, where the conduction-band population plays the role of the free-electron density. However, unlike in atomic gases, the optical response in a solid is not determined solely by electrons injected into the conduction band. The corresponding holes remaining in the valence band also undergo intraband motion and contribute simultaneously to the total intraband current. As a consequence, the physically meaningful quantity is not the current associated with the conduction band alone, but the total semiconductor current containing both electron and hole contributions as in Eq. (S13). This distinction is also essential from the viewpoint of gauge invariance. In a periodic solid, the intraband current associated with the conduction band alone is generally gauge dependent, because the separation between conduction- and valence-band contributions depends on the phase choice of the Bloch states. However, when the conduction-band electron and valence-band hole contributions are combined consistently, the total intraband polarization current becomes gauge invariant.

Therefore, the polarization-current formula for continuum free electrons in atomic media, Eq. (S23), corresponds naturally to the intraband polarization current in solids, Eq. (S13). Both include a conventional current that originates from the field-driven motion of carriers after excitation. In solids, this term is $\mathbf{J}_{\text{intra}}^{\text{conv}}(t) = q_e \sum_{n,\boldsymbol{k}} \rho_{nn}(\boldsymbol{k},t)\boldsymbol{v}_n(\boldsymbol{k})$, whereas in atomic gases it is $q_e n_e(t)\mathbf{v}(t)$. It should be noted that the second term in Eq. (S13), associated with the anomalous velocity, has no counterpart in atomic media.

The relation between the third term in Eq. (S13) and the first term in Eq. (S23) can be made explicit in a Wannier representation where the interband transition matrix element can be written as

$$\boldsymbol{\xi}_{nm}(\mathbf{k}) = \sum_{\ell} \boldsymbol{\xi}_{nm}^{(\ell)} e^{-i\mathbf{k}\cdot\mathbf{x}_\ell}, \tag{S25}$$

where $\mathbf{x}_\ell$ denotes a lattice-vector separation between the electron and the hole after a transition $m \to n$ where an electron emerges in the conduction band with ℓ lattice cells away from the hole left behind. In a single channel, $\mathbf{x}_\ell$ corresponds to $\mathbf{x}_0$ in the atomic gas case.

Then Eq. (S18b) satisfies

$$i\left[\boldsymbol{E}(t)\cdot\boldsymbol{\xi}_{nm}\right]_{;\boldsymbol{k}} = \sum_{\ell} \boldsymbol{R}_{nm}^{(\ell)}(\boldsymbol{k})\left[\boldsymbol{E}(t)\cdot\boldsymbol{\xi}_{nm}^{(\ell)}\right] e^{-i\boldsymbol{k}\cdot\boldsymbol{x}_\ell}, \tag{S26}$$

where

$$\boldsymbol{R}_{nm}^{(\ell)}(\boldsymbol{k}) = \boldsymbol{x}_\ell + \boldsymbol{\xi}_{nn}(\boldsymbol{k}) - \boldsymbol{\xi}_{mm}(\boldsymbol{k}) \tag{S27}$$

is the gauge-covariant electron–hole birth displacement associated with this transition channel.

The channel-resolved population-transfer rate is

$$\dot{\rho}_{nn;m}^{(\ell)}(\boldsymbol{k},t) = 2\,\mathrm{Im}\left[\rho_{nm}(\boldsymbol{k},t)\boldsymbol{E}(t)\cdot\boldsymbol{\xi}_{nm}^{(\ell)} e^{-i\boldsymbol{k}\cdot\boldsymbol{x}_\ell}\right], \tag{S28}$$

where the subscript $nn;m$ denotes population transfer into band n from band m.

The intraband mixed term can therefore be written as

$$\boldsymbol{J}_{\mathrm{intra}}^{\mathrm{inj-like}}(t) = -\frac{q_e^2}{\hbar} \sum_{(n,m)} \sum_{\boldsymbol{k},\ell} \boldsymbol{R}_{nm}^{(\ell)}(\boldsymbol{k}) \dot{\rho}_{nn;m}^{(\ell)}(\boldsymbol{k}, t). \tag{S29}$$

Equivalently, for an arbitrary detected current component α,

$$J_{\mathrm{intra},\alpha}^{\mathrm{inj-like}}(t) = -\frac{q_e^2}{\hbar} \sum_{(n,m)} \sum_{\boldsymbol{k},\ell} R_{nm,\alpha}^{(\ell)}(\boldsymbol{k}) \dot{\rho}_{nn;m}^{(\ell)}(\boldsymbol{k}, t). \tag{S30}$$

Comparing Eq. (S29) with the phenomenological injection-current expression in ionizing media, namely the first term in Eq. (S23), shows that the field-parallel component of the intraband polarization contains the same formal structure as the injection-current formula. Here, $\dot{\rho}_{nn;m}^{(\ell)}(\boldsymbol{k}), t)$ plays the role of the channel- and momentum-resolved carrier-injection rate, while $\boldsymbol{R}_{nm}^{(\ell)}(\boldsymbol{k})$ is the corresponding gauge-covariant electron–hole birth displacement. The important difference is that, in a periodic solid, the birth displacement is a gauge-covariant quantity containing both the intercell Wannier displacement and the intracell Berry-connection contribution.

As shown in Supplementary Note 1, the injection-current-like term that appears in the intraband polarization current has an equal-and-opposite counterpart in the interband polarization current. For a linearly polarized driving field, the two terms cancel exactly in the current projected along the laser polarization. For current components perpendicular to the laser polarization, a residual mixed term may in principle remain in a general multiband system. Such a term, however, belongs to the transverse geometric response, together with the self-commutator terms discussed above, and has the same transverse character as the anomalous velocity. It therefore contributes mainly to emission perpendicular to the laser polarization and to symmetry-allowed even-order harmonics. Therefore, the tunnelling-injection-like contribution does not survive as an independent radiation channel for the observed 3H and 5H signals.

Supplementary Note 3 | Direction-dependent field-strength scaling of intraband harmonics

To further examine whether the intensity-driven loss of angular contrast can be compatible with an intraband origin, we calculated the field dependence of the low-order harmonic yield along the Γ–M and Γ–K directions. At moderate field strengths, the relative weights of the two directions evolve rapidly, and the directional contrast is strongly reduced over the experimentally accessible range, giving rise to an effectively isotropic low-order response.

Crucially, the calculated isotropization is not monotonic. When the driving field is increased further, the directional contrast re-emerges and the low-order harmonics evolve back from near isotropy to pronounced anisotropy. The isotropic regime should therefore be understood as an intermediate strong-field window of intraband dynamics rather than as a criterion for excluding an intraband origin. In the present experiment, this re-entrant anisotropic regime lies beyond the damage threshold of the crystal and is therefore not experimentally accessible. This explains why the measured evolution terminates in the near-isotropic regime, while the full theoretical trend shows that isotropy alone cannot be used to rule out intraband radiation.

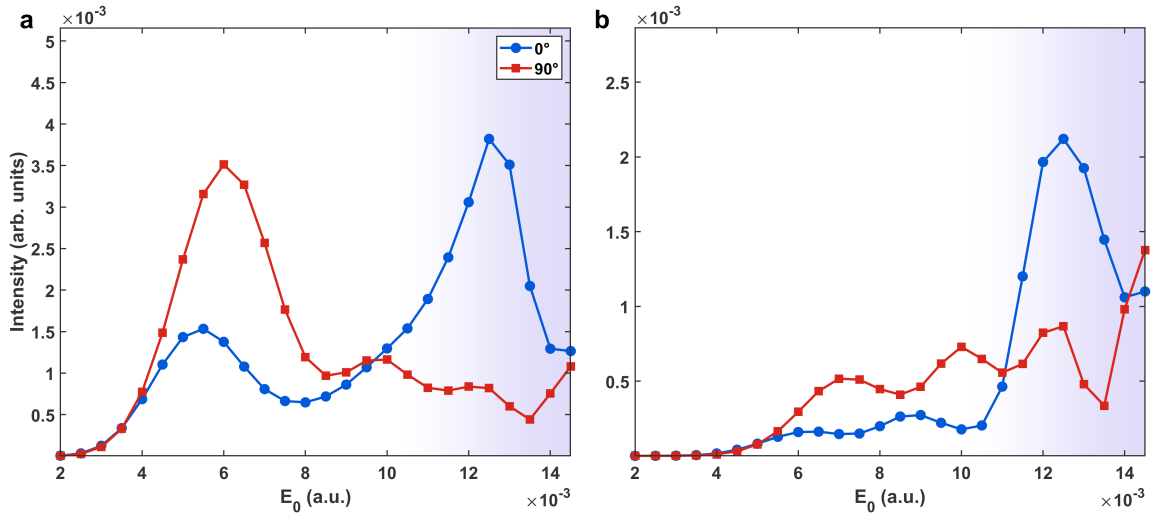

Fig. S 1: **Direction-dependent field scaling of intraband harmonics. a,b,** Calculated intensity of the intraband third harmonic (3H) and fifth harmonic (5H), respectively, as a function of field strength. In both panels, the blue and red curves correspond to the two orthogonal crystal orientations, labelled as 0° and 90°, respectively. Over the experimentally accessible range, the directional contrast is strongly reduced, giving rise to an effectively isotropic response. At still higher fields, however, the theory predicts a re-emergence of anisotropy, showing that isotropization is an intermediate strong-field regime of intraband dynamics rather than a criterion for excluding it. This re-entrant anisotropic regime lies beyond the damage threshold of the crystal and is therefore not accessible in the present experiment.

Supplementary Note 4 | Intraband calculation of the nonlinear indicator m

The 2020 *Nature Physics* work on amorphous quartz reported a large effective nonlinear indicator m, which was interpreted as an important signature of tunnelling-induced injection dynamics [7]. Here, we test whether this nonlinear behaviour can also be reproduced within an intraband picture. To this end, we evaluate m from the polarization-derived intraband response obtained from our SBE simulations.

The isotropic effective two-band model used here is intended as a minimal mechanism test rather than a full material-specific description of fused silica. Since fused silica is amorphous, no fixed crystallographic axis is expected to dominate the macroscopic response. We therefore choose parabolic conduction and valence bands together with an isotropic optical coupling in k space. This model retains the essential ingredients needed to evaluate the nonlinear indicator m: a wide band gap, field-driven intraband motion, and the same one-probe signal-extraction procedure used in the experiment. At the same time, it avoids building in any crystalline anisotropy or specially engineered anisotropic dipole structure by hand. The conduction-band minimum and valence-band maximum are separated by a direct band gap $E_g = 7.5$ eV at $k = 0$.

To preserve the isotropic character of this effective model, the off-diagonal Berry-connection matrix element, which plays the role of the interband transition dipole, was chosen as a real

radial vector field in $\mathbf{k}$ space,

$$C_{\mathrm{form}}(k) = \sqrt{\frac{E_p^{\xi}}{2[\Delta\varepsilon(k)]^2}}, \tag{S31}$$

$$\xi_{cv,x}(\mathbf{k}) = C_{\mathrm{form}}(k)\frac{k_x}{\sqrt{k^2 + k_{\mathrm{reg}}^2}}, \tag{S32}$$

$$\xi_{cv,y}(\mathbf{k}) = C_{\mathrm{form}}(k)\frac{k_y}{\sqrt{k^2 + k_{\mathrm{reg}}^2}}. \tag{S33}$$

This form ensures that $\boldsymbol{\xi}_{cv}(\mathbf{k})$ transform isotropically under in-plane rotations and avoids selecting any preferred crystalline direction. The small parameter k_{reg} regularizes the coupling near $k = 0$, while $C_{\mathrm{form}}(k)$ sets the magnitude of the transition matrix element through the band separation.

The intraband current is then calculated numerically from the SBE simulations for the two probe polarities and for the two polarization geometries. Following the same one-probe extraction strategy used in the analysis of the nonlinear signal, we isolate the component linear in the weak probe field through

$$J_{1\mathrm{p},\alpha}(t) = \frac{J_{\alpha}^{(+\mathrm{probe})}(t) - J_{\alpha}^{(-\mathrm{probe})}(t)}{2}, \tag{S34}$$

where $\alpha \in \{x, y\}$. After subtracting the mean value, applying a Gaussian window, and Fourier transforming the one-probe current, the intraband spectral yield is obtained as

$$I_{\alpha}^{\mathrm{intra}}(q) \propto \omega^2 \left|\mathcal{F}\left[w(t)J_{1\mathrm{p},\alpha}(t)\right]\right|^2, \tag{S35}$$

with $q = \omega/\omega_{\mathrm{pump}}$. The nonlinear indicator shown in Fig. 4e of the main text is finally defined from the integrated yields around the mixed-frequency channel $q_{\mathrm{target}} = 4.6$,

$$Y_{\parallel,\perp}^{\mathrm{intra}} = \int_{q_{\mathrm{target}}-\Delta q}^{q_{\mathrm{target}}+\Delta q} I_{\parallel,\perp}^{\mathrm{intra}}(q)\,\mathrm{d}q, \tag{S36}$$

$$m_{\mathrm{intra}} = \sqrt{\frac{Y_{\parallel}^{\mathrm{intra}}}{Y_{\perp}^{\mathrm{intra}}}}. \tag{S37}$$

The calculations were performed with a two-colour laser field consisting of a pump pulse at 2100 nm and a probe pulse at 800 nm, with pulse durations of 20 and 17 optical cycles, respectively. The dephasing time was set to $T_2 = T_{\mathrm{pump}}/4$, where T_{pump} is the optical period of the pump field. For the intensity scan in Fig. 4e, the pump intensity was varied from 2 to 16 TW cm^{-2}, while the probe intensity was kept fixed at 1.5×10^{-3} TW cm^{-2}.

As shown in Fig. 4e, the calculated m_{intra} obtained from the conventional intraband current follows the experimental trend and shows overall good agreement with the reported values over the scanned pump-intensity range. This comparison demonstrates that the large effective nonlinear response is not unique to an injection-current mechanism, but can also emerge from the intraband response.

Supplementary Note 5 | Influence of dephasing time on the delay-dependent intra- and interband responses

The dephasing time T_2 is commonly introduced in the semiconductor Bloch equations as a phenomenological parameter describing the decay of the interband coherence [1,10,11]. In a two-band model, this is usually implemented as a relaxation term for the off-diagonal density-matrix

element,

$$\left.\frac{d\rho_{cv}(\mathbf{k},t)}{dt}\right|_{\text{deph}} = -\frac{\rho_{cv}(\mathbf{k},t)}{T_2},$$

where ρ_{cv} denotes the interband coherence. This term is introduced phenomenologically in order to approximately account for many-body effects which lead to a decay of the coherent interband polarization by scattering, e.g., with phonons or between the photoexcited carriers.

However, inserting this phenomenological dephasing term into the coupled semiconductor Bloch equations does not affect only the interband polarization. Although T_2 is introduced explicitly as a decay of the interband coherence, the coherence and band populations are dynamically coupled by the optical field. As a result, the dephasing term can feed back into the population dynamics and thereby modify the calculated intraband polarization current and intraband harmonic emission. Such changes should not be interpreted as a microscopic relaxation model for intraband motion, since no separate intraband scattering mechanism has been introduced. Rather, they reflect the specific phenomenological prescription used to include interband dephasing in the coupled density-matrix dynamics.

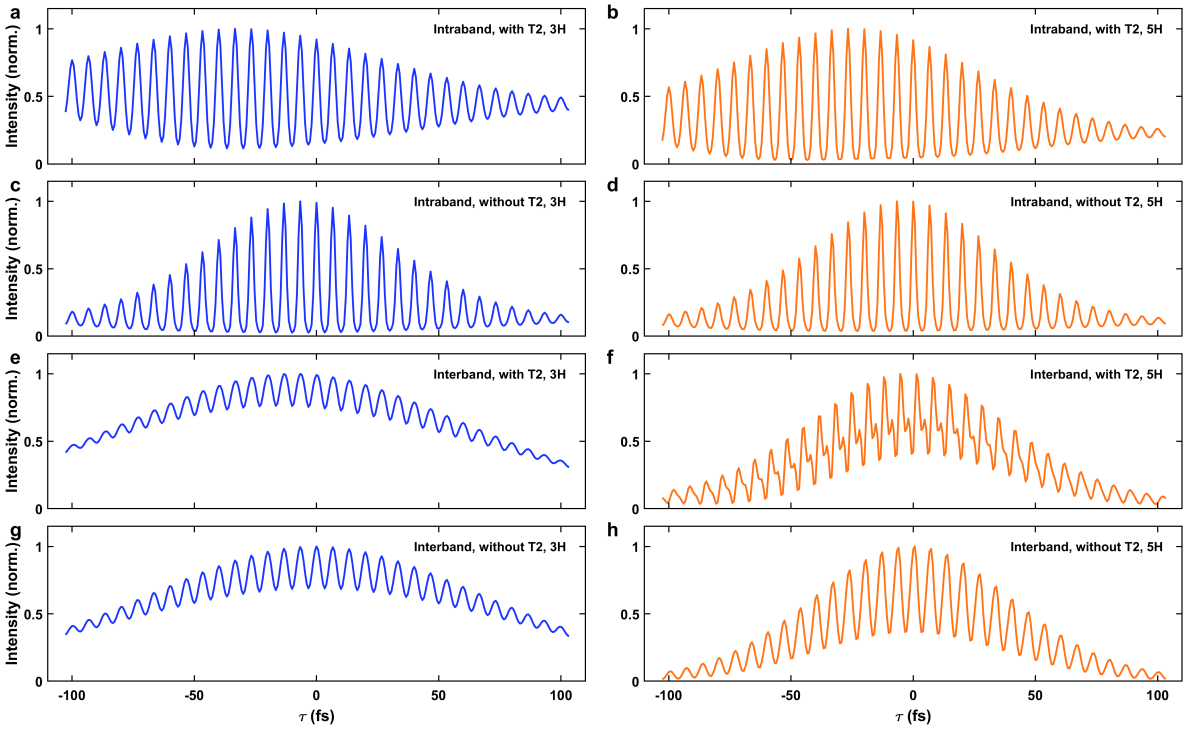

Fig. S 2: **Delay-dependent intra- and interband calculations with and without dephasing. a,b,** Intraband delay traces for the 3H and 5H channels calculated with a phenomenological dephasing time $T_2 = T_0/4$, where T_0 is the optical period of the fundamental driving field. **c,d,** Corresponding intraband delay traces calculated without phenomenological dephasing by setting $1/T_2 = 0$. **e,f,** Interband delay traces for the 3H and 5H channels calculated with $T_2 = T_0/4$. **g,h,** Corresponding interband delay traces calculated without phenomenological dephasing. All signals are plotted as normalized integrated intensities as a function of the pump–probe delay τ. For the intraband response, finite T_2 retains the subcycle modulation but introduces an asymmetric delay envelope and an anomalous one-sided enhancement, whereas the calculation without T_2 gives a more symmetric envelope. For the interband response, changing T_2 modifies the envelope and modulation contrast, but the signal remains broad and perturbative-like and does not reproduce the high-contrast intraband switching observed experimentally.

We therefore examined how the phenomenological interband dephasing time affects the delay-

dependent HHG response. Figure S3 compares the calculated 3H and 5H signals obtained with $T_2 = T_0/4$, where T_0 is the optical period of the fundamental field, and in the coherent limit $T_2 \to \infty$. For the intraband diagnostic, imposing a finite interband-coherence dephasing time does not remove the subcycle modulation, but it strongly distorts the delay envelope: the response develops an asymmetric, one-sided enhancement and is displaced away from the temporal overlap of the two driving pulses. Such an envelope distortion is not observed experimentally. By contrast, the coherent intraband calculation preserves the subcycle modulation and gives a more symmetric delay envelope centred near temporal overlap, consistent with the measured delay-dependent response. We have tested other finite values of T_2 and find the same type of envelope distortion, indicating that it originates from the phenomenological dephasing prescription rather than from the intrinsic intraband dynamics.

For this reason, the intraband results discussed in the main text are obtained from the coherent Bloch equations, without imposing an interband-coherence T_2 on the intraband diagnostic. This choice does not assume that relaxation is absent in the material. Rather, it avoids attributing artificial distortions introduced by a phenomenological interband-dephasing term to the subcycle intraband response. The coherent intraband calculation is used to isolate the intrinsic field-driven intraband motion responsible for the observed half-cycle, high-contrast harmonic switching.

The interband contribution is treated differently because the interband polarization is directly governed by the decay of interband coherence. We therefore use a finite T_2 for the interband calculation as a standard phenomenological estimate of the dephasing-limited interband polarization. We also compare interband responses with and without T_2 in Fig. S3; in both cases the signal remains broad and perturbative-like and does not reproduce the high-contrast subcycle switching. Thus, the different use of T_2 in the two diagnostic calculations reflects the distinct physical roles of coherence decay in the intra- and interband responses. It is used for channel identification, not to construct a single dissipative total current from two different relaxation models.

References

1. Vampa, G. et al. Theoretical analysis of high-harmonic generation in solids. *Phys. Rev. Lett.* **113**, 073901 (2014).

2. Golde, D., Meier, T. & Koch, S. W. High harmonics generated in semiconductor nanostructures by the coupled dynamics of optical inter- and intraband excitations. *Phys. Rev. B* **77**, 075330 (2008).

3. Resta, R. Macroscopic polarization in crystalline dielectrics: the geometric phase approach. *Rev. Mod. Phys.* **66**, 899–915 (1994).

4. Spaldin, N. A. A beginner's guide to the modern theory of polarization. *J. Solid State Chem.* **195**, 2–10 (2012).

5. Aversa, C. & Sipe, J. E. Nonlinear optical susceptibilities of semiconductors: results with a length-gauge analysis. *Phys. Rev. B* **52**, 14636–14645 (1995).

6. Geissler, M., Tempea, G., Scrinzi, A., Schnürer, M., Krausz, F. & Brabec, T. Light propagation in field-ionizing media: extreme nonlinear optics. *Phys. Rev. Lett.* **83**, 2930–2933 (1999).

7. Jürgens, P. et al. Origin of strong-field-induced low-order harmonic generation in amorphous quartz. *Nat. Phys.* **16**, 1035–1039 (2020).

8. Brunel, F. Harmonic generation due to plasma effects in a gas undergoing multiphoton ionization in the high-intensity limit. *J. Opt. Soc. Am. B* **7**, 521–526 (1990).

9. Babushkin, I. et al. All-optical attoclock for imaging tunnelling wavepackets. *Nat. Phys.* **18**, 417–422 (2022).

10. Silva, R. E. F., Martín, F. & Ivanov, M. High harmonic generation in crystals using maximally localized Wannier functions. *Phys. Rev. B* **100**, 195201 (2019).

11. Cavaletto, S. M., Kowalczyk, K. M., Navarrete, F. O. & Rivera-Dean, J. The attoscience of strong-field-driven solids. *Nat. Rev. Phys.* **7**, 38–49 (2025).